Progress In Electromagnetics Research B, Vol. 70, 41–53, 2016

Sliding Spotlight Bistatic Synthetic Aperture Radar Image Formation Algorithm Based on Direct-Path Signal Compensation

Feifei Yan*, Wenge Chang, Xiangyang Li, and Qilei Zhang

Abstract—In fixed-receiver bistatic synthetic aperture radar (SAR), the spaceborne SAR is used as an illuminator. The direct-path signal and bistatic SAR raw data are sampled by the fixed-receiver which is placed on the top of a building or a hill. As the direct-path signal has high signal-to-noise ratio (SNR) advantage and almost the same synchronization error terms, it is used as the reference signal for the range matched filtering. Then the range compression can be realized with a time and frequency synchronization process. However, after range match filtering by the direct-path signal, the range history of point target consists of three square-root terms, for which it is hard to use the Principle of Stationary Phase (POSP). Meanwhile, the two-dimensional (2-D) spatial variation of the target's 2-D frequency spectrum is serious. By combining azimuth preprocessing, direct-path signal compensation and nonlinear Chirp Scaling (NLCS) imaging algorithm, a new focusing algorithm is presented in this paper. Simulation results of point targets are presented to validate the efficiency and feasibility of the proposed imaging algorithm. Finally, this algorithm is also validated by the measured data which is obtained using the HITCHHIKER system.

1. INTRODUCTION

Synthetic aperture radar (SAR) is a microwave imaging tool for remote sensing. It can acquire high resolution images of the scene in all weather conditions. In a fixed-receiver bistatic SAR system, the receiver is fixed on the ground or on a building, and the transmitter is usually mounted on the spaceborne platform. It is benefitial in terms of low-cost, higher operational flexibility, etc. These features make it irreplaceable for both civil and military services.

Time and frequency synchronization is a big challenge in a bistatic SAR system. Taking into account the high signal-to-noise ratio (SNR) advantage and almost the same synchronization error terms, the direct-path data are used as the reference signal for range matched filtering [1, 2]. Then the time and frequency synchronization errors of the bistatic SAR raw data can be eliminated precisely. However, by observing the analytical equation of the synchronized signal, it can be seen that the range history consists of three square-root terms, which means that it is hard to get the two-dimensional (2-D) frequency spectrum. Usually, time-domain imaging method is used to realize the focusing of the scene. However, this method suffers from severe computational load.

Based on the Method of Series Reversion (MSR), a range-Doppler imaging algorithm is proposed in sliding spotlight bistatic SAR [3]. By using the 2-D Principle of Stationary Phase (POSP), two Doppler-based monostatic imaging algorithms, range-Doppler algorithm and Chirp Scaling algorithm, are implemented to deal with the moderate-squint azimuth-variant bistatic SAR data [4]. Based on the 2-D inverse Scaling Fourier transform, a frequency-domain imaging algorithm of the spaceborne/airborne

Received 6 August 2016, Accepted 29 September 2016, Scheduled 14 October 2016

* Corresponding author: Feifei Yan (ddx.yff@gmail.com).
The authors are with the College of Electronic Science and Engineering, National University of Defense Technology, Changsha, Hunan 410073, P. R. China.

configuration is proposed in [5]. However, due to serious spatial variation of the point target after range compression with the direct-path signal, these imaging algorithms cannot be applied anymore.

In this paper, we are concerned with the frequency-domain imaging algorithm for the synchronized data using the mentioned method in fixed-receiver bistatic SAR. The transmitter is working in the sliding spotlight mode. Based on the preprocessing in azimuth direction, direct-path signal compensation and Nonlinear Chirp Scaling (NLCS) algorithm, a focusing algorithm is proposed. Then simulation experiments are performed to verify the efficiency and accuracy of the proposed method. Finally, the performance of the proposed method is also tested with the measured data of HITCHHKIER system [4].

The paper is arranged as follows. In Section 2, the geometry of a fixed receiver bistatic SAR and the proposed imaging algorithm are introduced. Simulation results and measured data results are presented in Section 3. Finally, in Section 4, the summary is presented.

2. GEOMETRY OF FIXED-RECEIVER BISTATIC SAR AND THE PROPOSED METHOD

In a fixed-receiver bistatic SAR system, the receiver has two receive channels. The first channel is dedicated to the acquisition of the direct-path signal. The second one is used to sample the bistatic SAR raw data of the scene.

The imaging geometry of the fixed-receiver bistatic SAR is shown in Figure 1. Here, a right-hand Cartesian coordinate system is used. The projection of the receiver is selected as the coordinate origin. The transmitter moves with velocity v_T along the Y axis, working in sliding spotlight mode [1]. The height of the fixed-receiver is H_R. The coordinate of point target P is $(x, y, 0)$. As shown in Figure 1, the bistatic range of P can be written as

$$r_T(t_m) = \sqrt{r_{T0}^2 + v_T^2 (t_m - t_0)^2}, \quad t_0 = y\left(\frac{1}{v_T} - \frac{1}{v_{TF}}\right) \tag{1}$$

$$r_R(y) = \sqrt{r_{R0}^2 + y^2} \tag{2}$$

where t_m is the slow time and v_{TF} the velocity of the transmitter's beam footprint. r_{T0} and r_{R0} are the closest distances from the transmitter and the receiver to the target, respectively.

During the synthetic aperture time of P, the range history of the direct-path signal can be written as

$$r_D(t_m) = \sqrt{r_{D0}^2 + v_T^2 (t_m + t_1)^2}, \quad t_1 = \frac{y}{v_T} \tag{3}$$

where t_1 is the time when the distance from the transmitter to the target P is the closest distance r_{D0}.

Assume that the transmitter signal is a linear frequency modulation (LFM) signal. After quadrature demodulation, the raw data of the fixed-receiver bistatic SAR system with time and frequency

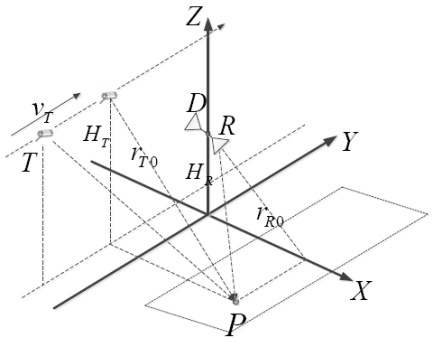

Figure 1. Fixed-receiver bistatic SAR system.

synchronization errors can be written as

$$s_r(t_m,\tau)=\sigma_p\omega_a(t_m-t_0)\,\omega_r\left(\tau-\frac{r_T(t_m)+r_R(y)}{c}-e(t_m)\right)\exp(j\phi_e(t_m))$$
$$\times\exp\left(j\pi k_r\left(\tau-\frac{r_T(t_m)+r_R(y)}{c}-e(t_m)\right)^2\right)\times\exp\left(-j2\pi f_0\left(\frac{r_T(t_m)+r_R(y)}{c}+e(t_m)\right)\right) \quad (4)$$

where τ is the fast time, σ_p the terrain reflectivity at P, k_r the chirp rate, f_0 the carrier frequency. $e(t_m)$ and $\phi_e(t_m)$ describe the time and frequency synchronization errors, respectively. ω_r and ω_a are the antenna beam patterns in the range and azimuth direction, respectively.

According to Eq. (4), the time synchronization error $e(t_m)$ introduces an increasing range displacement. $\phi_e(t_m)$ is a phase error varied with the slow time [6]. Therefore, the quality of bistatic SAR image will be degraded by the time and phase synchronization errors. To improve the focusing performance of imaging algorithm, some time and phase synchronization compensation techniques should be performed.

Supposing that the direct-path channel and the bistatic SAR raw data channel are balanced in advance, both channels' signals suffer from the same time and phase synchronization errors. After quadrature demodulation, the direct-path signal can be expressed by

$$s_d(t_m,\tau)=\omega_r\left(\tau-\frac{r_D(t_m)}{c}-e(t_m)\right)\exp\left(j\pi k\left(\tau-\frac{r_D(t_m)}{c}-e(t_m)\right)^2\right)$$
$$\times\exp\left(-j2\pi f_0\left(\frac{r_D(t_m)}{c}+e(t_m)\right)\right)\exp(j\phi_e(t_m)) \quad (5)$$

After range match filtering by the direct-path signal, the bistatic SAR raw data can be written as [2]

$$s(t_m,\tau)=\sigma_p\omega_a(t_m-t_0)\,\omega_r\left(\tau-\frac{r(t_m)}{c}\right)\exp\left(-j2\pi\frac{r(t_m)}{\lambda}\right) \quad (6)$$

where $\lambda=c/f_0$ is the wavelength and $r(t_m)$ the range history of point target after range match filtering by the direct-path signal

$$r(t_m)=r_T(t_m)+r_R(y)-r_D(t_m) \quad (7)$$

As can be seen from Eqs. (6) and (7), after range match filtering by the direct-path signal, the synchronization errors can be eliminated precisely during the range compression. However, the range history of point target is composed of three square-root terms, which is hardly to be resolved.

2.1. Two-Dimensional Spatial Variation of Spectrum

Since $r(t_m)$ consists of three square-root terms, it is hard to use the POSP. To obtain the 2-D frequency spectrum of the bistatic SAR raw data, the phase terms of Eq. (6) is expanded by Taylor series expansion, and then we can get

$$r_T(t_m)=K_{T0}+K_{T1}t_m+K_{T2}t_m^2+\ldots \quad (8)$$
$$r_D(t_m)=K_{D0}+K_{D1}t_m+K_{D2}t_m^2+\ldots \quad (9)$$

where

$$K_{T0}=\sqrt{r_{T0}^2+v_T^2t_{T0}^2},\quad K_{T1}=-\frac{v_T^2t_{T0}}{\sqrt{r_{T0}^2+v_T^2t_{T0}^2}},\quad \ldots \quad (10)$$

$$K_{D0}=\sqrt{r_{D0}^2+v_T^2t_{D0}^2},\quad K_{D1}=-\frac{v_T^2t_{D0}}{\sqrt{r_{D0}^2+v_T^2t_{D0}^2}},\quad \ldots \quad (11)$$

Then $r(t_m)$ can be written as

$$r(t_m)=\mu_0+\mu_1t_m+\mu_2t_m^2+\mu_3t_m^3+\mu_4t_m^4+\ldots \quad (12)$$

where

$$\mu_0 = K_{T0} + r_R(t_{T0}, r_{T0}) - K_{D0}, \quad \mu_1 = K_{T1} - K_{D1}, \quad \ldots \tag{13}$$

Based on the MSR and keeping the terms up to a fourth-order term, the 2-D frequency spectrum of Eq. (6) can be deduced and expressed as

$$S(f_\tau, f_a) = W_r(f_\tau) W_a(f_a) \exp(j\phi(f_\tau, f_a)) \tag{14}$$

Ignoring the high order terms of f_τ and f_a, $\phi(f_\tau, f_a)$ can be written as

$$\phi(f_\tau, f_a) \approx \phi_c + \phi_0(f_a, r) + \phi_1(f_a, f_\tau, r) + \phi_2(f_a, f_\tau, r) \tag{15}$$

where r is the range position of point target.

The detailed expressions of the four phase terms in Eq. (15) can be found in [7]. The first term is a residual phase which is irrelevant to f_τ and f_a, so it has no effect on the focusing result. $\phi_0(f_a, r)$ is the azimuth modulation term which is irrelevant to f_τ. The third term in Eq. (15) represents the range cell migration (RCM) which is linearly dependent on f_τ. The fourth term in Eq. (15) is a range and azimuth coupling phase.

Usually, the 2-D coupling phase term $\phi_2(f_a, f_\tau, r)$ is weakly range dependent, so it can be compensated by the reference range, and it is sufficient for the whole scene [7].

Figure 2 shows the residual phase of point target (azimuth: 1000 m) after compensated by the reference point target. As can be seen from Figure 2, if the 2-D coupling phase is compensated by the reference range, the residual phase of the marginal target is too big to realize the focusing of the scene. So the targets suffer from serious spatial variation after range compressed by the direct-path signal.

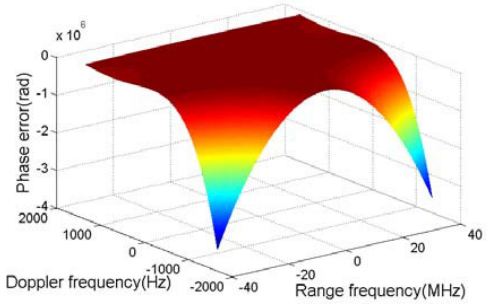

Figure 2. Residual phase of marginal point target.

To realize the focusing of the scene and decrease the complexity of the range history in Eq. (7), the accurate range history of the direct-path signal is estimated, and the terms of the direct-path signal in Eq. (6) are eliminated by phase compensated along the azimuth direction. Finally, the NLCS image algorithm is used to realize the focusing of the bistatic SAR raw data.

2.2. Range History of the Direct-Path Signal

According to the orbit information of the satellite, the range history of the direct-path signal can be expressed by a fourth-order polynomial expansion [8]

$$r_D(t_m) = a_0 + a_1 t_m + a_2 t_m^2 + a_3 t_m^3 + a_4 t_m^4 \tag{16}$$

where a_i, $i = 0 \sim 4$ are the polynomial coefficients which can be estimated from the orbital information [8].

The zero Doppler time (ZDT) t_0 is defined at which $r_D(t_m)$ has a minimum value and $dr_D(t_m)/dt_m = 0$. If the real ZDT is nonzero and defined by t_0, then the real range history of the direct-path signal is

$$r'_D(t_m) = r_D(t_m - t_0) \tag{17}$$

Substituting $t_m - t_0$ in Eq. (16), $r'_D(t_m)$ can be expressed by a new fourth-order polynomial

$$r'_D(t_m) = a'_0 + a'_1 t_m + a'_2 t_m^2 + a'_3 t_m^3 + a'_4 t_m^4 \tag{18}$$

where

$$\begin{aligned} a'_0 &= a_4 t_0^4 - a_3 t_0^3 + a_2 t_0^2 - a_1 t_0 + a_0 \\ a'_1 &= 4a_4 t_0^3 + 3a_3 t_0^2 - 2a_2 t_0 + a_1 \\ a'_2 &= 6a_4 t_0^2 - 3a_3 t_0 + a_2 \\ a'_3 &= -4a_4 t_0 + a_3 \\ a'_4 &= a_4 \end{aligned} \tag{19}$$

From Eq. (19), it can be seen that the third-order polynomial coefficient is, in relative terms, very sensitive to t_0. Therefore, t_0 can be estimated by

$$t_0 = \frac{a_3 - a'_3}{4a_4} \tag{20}$$

Based on the polynomial fit of the direct-path signal's peak phase, a method to estimate t_0 is proposed in [8], and then the real range history $r'_D(t_m)$ of the direct-path signal can be obtained.

However, due to phase noise, there is a ZDT estimate error. Let us denote the ZDT estimate error by Δt_0. After compensation with the estimated range history $r'_D(t_m - \Delta t_0)$, the bistatic SAR raw data can be expressed as

$$s_1(\tau, t_m) = \sigma_p \omega_r \left(\tau - \frac{r(t_m)}{c}\right) \exp\left(-j2\pi \frac{r(t_m)}{\lambda}\right) \tag{21}$$

where

$$r(t_m) = r_T(t_m) + r_R(y) + r'_D(t_m) - r'_D(t_m - \Delta t_0) = r_T(t_m) + r_R(y) + \Delta r_D(t_m) \tag{22}$$

According to Eqs. (21) and (22), it can be seen that the ZDT estimate error results in not only the RCM error $\Delta r_D(t_m)/c$, but also the distortion of peak phase error $\exp(-j2\pi f_0 \Delta r_D(t_m)/c)$ along the azimuth direction. The effects of the two errors are derived analytically below.

(1) RCM error
According to the simulated parameters list in Table 1, the RCM error is shown in Figure 3.
As can be seen from Figure 3, the RCM error changes linearly with the ZDT error. When 1/4 of the range sampling interval is used as the RCM error lower bound, the estimated error of ZDT should smaller than 0.02 s.

(2) Peak phase error in azimuth direction
According to Eqs. and (17), the peak phase error can be analytically described by a linear superposition of four different components: constant phase, linear phase, quadratic phase and high frequency phase

$$\phi(t_m) = \phi_c + 2\pi k_1 t_m + \pi k_2 t_m^2 + \Delta\phi \tag{23}$$

where ϕ_c is the constant phase which has no influence on the image. k_1 and k_2 are the coefficients of linear phase and quadratic phase, respectively. $\Delta\phi = \pi k_3 t^3 + \pi k_4 t_m^4 + \ldots$ is the high frequency phase.

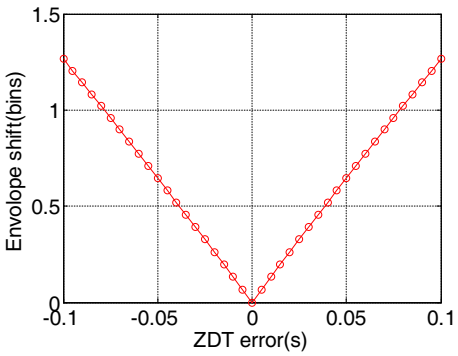

Figure 3. RCM error.

Since the phase error not only defocuses the SAR image but also causes spurious sidelobes in the impulse function, an analysis of the phase errors is necessary [9].

(a) The linear phase will cause a shift of the bistatic impulse response in azimuth direction. The azimuth shift is given by $\Delta x' = k_1 v_T / k_a$ in [9]. k_a is the Doppler frequency modulation rate.

(b) The quadratic phase will cause a widening of the azimuth response and phase error. For a bistatic SAR, this error can be approximated by quadratic phase errors: QPE $= \pi k_2 T_{syn}^2 / 4$.

(c) High frequency phase will cause spurious sidelobes in the impulse response function. If the estimate error of the ZDT is 0.1 s, then $k_3/k_a \approx 3.95\text{e}-6$, so the influence of the high frequency phase on the azimuth focusing can be ignored.

The influences of the linear and quadratic phase errors are shown in Figure 4.

As can be seen from Figure 4(a), the linear phase will introduce a drift in azimuth direction. Figure 4(b) shows that the QPE varies with the estimate error of ZDT. A typical requirement of QPE is QPE $< \pi/4$ which leads to a resolution loss of 10% in azimuth processing [9]. In this example, the QPE can be ignored.

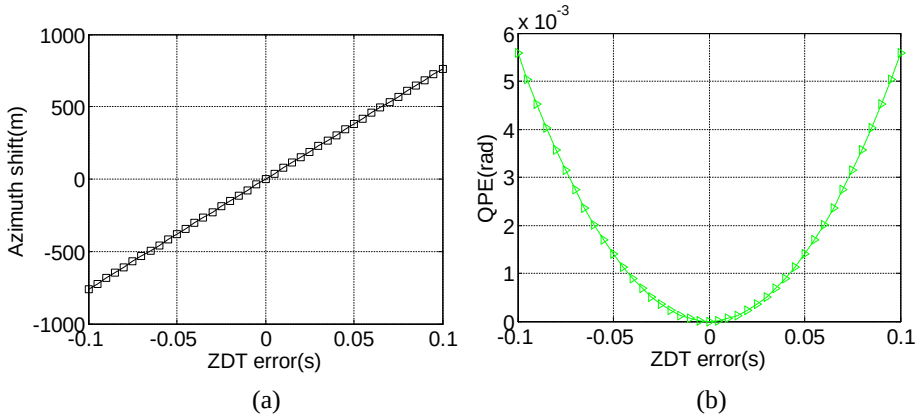

Figure 4. Influences of the phase errors. (a) Azimuth shift. (b) QPE.

2.3. The Proposed Imaging Algorithm

In a sliding spotlight bistatic SAR system, the steering of the transmitter's antenna beam results in the increase of the azimuth bandwidth and introduces a linear Doppler centroid varying with the azimuth position of the target. Usually, the Doppler centroid of marginal point target will be outside the PRF range. If the phase of the direct-path signal is compensated, then the bistatic SAR raw data will be aliased in azimuth Doppler frequency domain. Hence, the preprocessing in azimuth direction should be performed before the image focusing [10]. After preprocessing in the azimuth direction, the signal $s_r(\tau, t'_m)$ is compensated by the phase terms of $r'_D(t_m)$, and then the NLCS imaging algorithm is used to realize the focusing of the scene [11, 12].

2.3.1. Azimuth Preprocessing

The reference signal for azimuth preprocessing can be expressed by

$$H_{ref}(t_a) = \exp\left(j\pi k_a t_m^2\right) \tag{24}$$

where $k_a = v_T^2/(\lambda r_{T0})$.

Convoluting the bistatic SAR raw data in Eq. (6) with the reference signal expressed in Eq. (24), we can get the following result

$$\begin{aligned} S_2\left(f_\tau, t'_m\right) &= \exp\left(j\pi k_a t'^2_m\right) \times \int S_r\left(f_\tau, x\right) \exp\left(j\pi k_a x^2\right) \exp\left(-j2\pi k_a t_m x\right) dx \\ &= H_{ref}\left(t'_m\right) \cdot \mathrm{FFT}\left[S_r\left(f_\tau, t_m\right) H_{ref}\left(t_m\right)\right] \end{aligned} \tag{25}$$

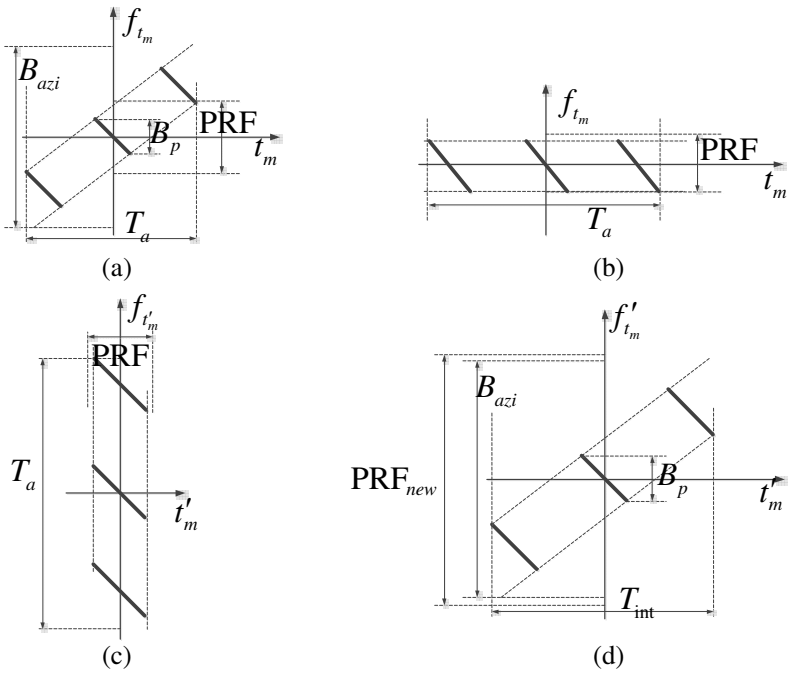

Figure 5. Azimuth preprocessing. (a) Bistatic SAR raw data. (b) After multiplied by the reference signal. (c) After convolution. (d) Result of azimuth preprocessing.

After being multiplied by the reference function, it can be seen from Figure 5(b) that the supporting area of the bistatic SAR raw data is confined in (Ta, PRF) in range-Doppler frequency domain. The integration in Eq. (25) can be seen as a fast Fourier transform (FFT) from the azimuth coordinate t_m to a new azimuth coordinate t'_m, which is shown in Figure 5(c). When the quadratic phase $H^*_{ref}(t'_m)$ is compensated in the new azimuth coordinate t'_m, the un-aliased raw data is shown in Figure 5(d).

The convolution of Eq. (25) in 2-D frequency domain can be rewritten as

$$S_2\left(f_\tau, f'_{t_m}\right) = S_r\left(f_\tau, f'_{t_m}\right) H_{ref}\left(f'_{t_m}\right) \tag{26}$$

where f'_{t_m} is the frequency variable corresponding to t'_m and $H_{ref}(f'_{t_m})$ the 2-D frequency spectrum of $H_{ref}(t'_m)$.

If the second term in the right side of Eq. (26) is compensated, we can finally get the bistatic SAR raw data $s_r(\tau, t'_m)$ without Doppler centroid aliasing.

2.3.2. Direct-Path Signal Compensation

After preprocessing in the azimuth direction, the bistatic SAR raw data $s_r(\tau, t'_m)$ are compensated by the phase terms of the estimated range history of the direct-path signal

$$s_{RC}\left(\tau, t'_m\right) = s_r\left(\tau, t'_m\right) \exp\left(-j2\pi \frac{f_c + f_\tau}{c} r'_D\left(t'_m\right)\right) \tag{27}$$

where $r'_D(t'_m)$ is the interpolation result of $r'_D(t_m)$ in the new coordinate t'_m.

After being compensated by the phase of direct-path signal, the serious spatial variation introduced by the direct-path signal can be eliminated. Then the bistatic SAR raw data can be written as

$$s_{RC}\left(\tau, t'_m\right) = \sigma_p \omega_r\left(\tau - \frac{r_T\left(t'_m\right) + r_R\left(y'\right) + \Delta r_D\left(t'_m\right)}{c}\right) \times \exp\left(-j2\pi f_0 \frac{r_T\left(t'_m\right) + r_R\left(y'\right) + \Delta r_D\left(t'_m\right)}{c}\right) \tag{28}$$

where $\Delta r_D(t'_m)$ is the residual range history term introduced by the estimate error of ZDT. Then the NLCS imaging algorithm is performed to realize focusing of the scene.

2.3.3. Perturbation Function

As the Doppler FM rates vary along the azimuth positions, the azimuth focusing cannot be handled using a single frequency domain filter. A perturbation function $h_{pert}(t'_m) = \exp(j\pi\alpha t'^4_m)$ is multiplied to the signal in azimuth direction. Then the Doppler frequency modulation rates are altered to the reference target. Therefore, after perturbation, the Doppler frequency modulation rate of target P is

$$K'_a(y_p) = \frac{1}{2\pi}\frac{d^2(\pi K_a(y_p)(t'_m - t_0)^2 + \pi\alpha t'^4_m)}{dt'^2_m}|_{t_m=t_0} = K_a(y_p) + 6\alpha t_0^2 \tag{29}$$

The Doppler frequency modulation rate in Eq. (29) should be equal to $K_a(0)$. Therefore, the coefficient α is given by

$$\alpha = -\frac{\Delta K_a(y_p)}{6t_0^2} = -\frac{K_a(y_p) - K_a(0)}{6t_0^2} \tag{30}$$

Expanding the exponential phase in Eq. (28) by second-order Taylor series, we have

$$s_{RC}(t'_m, \tau) \approx \sum \sin c\left(B\left(\tau - r\left(t'_m\right)/c\right)\right)\exp(-j\phi_0) \times \exp\left(j\pi K_a(y_p)(t'_m - t_0)^2\right) \tag{31}$$

where ϕ_0 is a constant phase.

The exponential phase of Eq. (31) can be written as

$$\varphi_{Ap} = \exp(j\pi K_a(y_p)(t'_m - t_0)^2 + j\pi\alpha t'^4_m)\exp(-j\phi_0) = \exp(j\pi K_a(0)(t'_m - t_0)^2)\cdot\exp(j\phi_\Delta)\exp(-j\phi_0) \tag{32}$$

where ϕ_Δ is the residual phase error after NLCS process.

2.3.4. RCM Correction (RCMC)

According to [11], the RCM difference between the closest point target and the marginal point target can be neglected. Therefore, the RCMC can be performed using r_{T0} as reference range. So the expression of RCMC is

$$H_{RCMC}(f_a, f_r) = \exp\left(j\pi\frac{r_{T0}}{c}\left(\frac{f_a}{f_{aM}}\right)^2 f_r\right) \tag{33}$$

2.3.5. Azimuth Focusing and Phase Compensation

As shown in Eq. (32), the Doppler frequency modulation rates of the targets have been equalized along the azimuth direction by NLCS process. However, a residual phase in Eq. (32) should be taken into account during the azimuth focusing. Setting $t = t'_m - t_0$, the residual phase can be expressed as

$$\phi_\Delta = \pi K_a(y_p)(t'_m - t_0)^2 + \pi\alpha t'^4_m - \pi K_a(0)(t'_m - t_0)^2 = \pi\alpha t^4 + 4\pi\alpha t^3 t_0 + 4\pi\alpha t t_0^3 + \pi\alpha t_0^4 \tag{34}$$

As can be seen from Eq. (34), there are four exponential terms. The first term is a quartic phase modulation which will bring the main-lobe broadening and the side-lobe raising. The second term is a cubic phase modulation, which will bring the asymmetry side-lobe. The third term is a linear term (Doppler shift), which will introduce a shift in the Doppler frequency domain, so different targets occupy different parts in the Doppler frequency domain. The last one is a constant phase term, which has no effect on the imaging processing.

In the spaceborne case, the amounts of the higher order phase terms are significant, which should be taken into account in the azimuth match filtering [11]. After azimuth Fourier transform, Eq. (34) can be expressed as

$$\phi_{\Delta f_a} \approx -\pi\frac{f_a^2}{K_a(0)} + \pi\alpha\left(\frac{f_a}{K_a(0)}\right)^4 + 4\pi\alpha\left(\frac{f_a}{K_a(0)}\right)^3 t_0 + 4\pi\alpha\frac{f_a}{K_a(0)}t_0^3 + \pi\alpha t_0^4 - 2\pi f_a t_0 \tag{35}$$

It should be pointed out that the derivation of the stationary point in Eq. (35) has ignored the high order phase terms and linear phase term. The quartic phase modulation is the same for all targets in the same range bin, and the compensation of that can be combined with the compensation of the quadratic phase modulation. However, the amounts of the cubic and linear phase modulation vary with

the azimuth position t_0. Therefore, the compensation of these phase terms cannot be applied using a single frequency domain matched filter. To overcome this difficulty, an effective sub-aperture approach is proposed to deal with the azimuth-dependent characteristic of the azimuth compression. The sub-aperture approach divides the echo into sub-apertures in time-domain and finds a frequency domain matched filter which compensates the cubic and linear phase modulation for each sub-aperture. The sub-aperture frequency domain matched filter is built using the center position of the sub-aperture as reference. After Inverse FFT, the sub-aperture data is focused well. At last, the focused sub-aperture images are combined to a whole image. It is necessary that there should be a little overlap (5%) between sub-apertures for the continuity of the phase.

The key of the sub-aperture approach is the division of the sub-aperture. In the case of large sub-aperture, the phase error is significant, which will deteriorate the image quality. If the sub-aperture is too small, the approach is inefficient. In this paper, we use $\pi/8$ as the cubic phase error lower bound

$$4\pi\alpha\left(\frac{T_{syn}}{2}\right)^3\frac{\Delta t_0}{2}\leq\frac{\pi}{8} \tag{36}$$

where T_{syn} is the synthetic aperture time

$$T_{syn}\approx\frac{r_{T0}\theta_T}{v_{TF}}=\frac{r_{T0}D_T}{\lambda v_{TF}} \tag{37}$$

where θ_T is the the transmitter's beamwidth and D_T the size of the transmitter's antenna.

Therefore, the sub-aperture Δt_0 should satisfy

$$\Delta t_0\leq\frac{1}{2\alpha T_{syn}^3}=\frac{1}{2\alpha}\left(\frac{r_{T0}D_T}{\lambda v_{TF}}\right)^3 \tag{38}$$

Figure 6 shows the main steps of the proposed imaging algorithm. Firstly, the azimuth preprocessing an direct-path signal compensation are performed. Then the NLCS transform is performed to equalize the Doppler frequency modulation rates in the azimuth direction. The azimuth compression algorithm consists of two steps: compensating the quadratic and quartic phase modulation in the whole aperture to realize coarse focus and compensating the cubic and linear phase modulation in sub-aperture to realize fine focus.

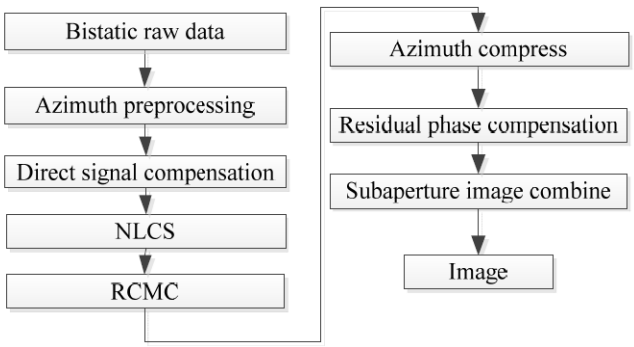

Figure 6. Main steps of the proposed imaging method.

3. VALIDATION TEST

Several simulations are carried out in this section to test the proposed imaging algorithm. First, simulations of point targets are performed to test the focusing accuracy of the proposed algorithm. Second, this imaging algorithm is validated with measured data obtained using HITCHHIKER system.

3.1. Simulation Results

Table 1 shows the simulation parameters. Several targets are arranged as a 3×5 matrix in the simulated scene.

Table 1. Simulation parameters.

Parameter	Value
H_T	514 km
r_{T0}	854 km
H_R	100 m
r_{R0}	1200 m
Transmitter velocity	7700 m/s
Transmitter's beam footprint velocity	2100 m/s
Center frequency	9.65 GHz
PRF	3224 Hz
Simulation bandwidth	30 MHz

The synchronization errors are listed in [13]. The real ZDT is set to 0.38 s. According to the simulation parameters in Table 1, the direct-path signal and the bistatic SAR raw data of point targets with time and frequency synchronization errors are generated. The direct-path signal is used to estimate the ZDT. As the analytical expression of the ZDT's estimate error is hard to obtain, the Monte Carlo simulations are performed to test the estimation precision of the ZDT. The Monte Carlo simulation is executed 100 times.

Figure 7(a) shows the estimation results of the ZDT. It is seen that the estimated value varies around the initial ZDT value. Figure 7(b) shows the estimation error of the ZDT. The maximum estimation error is less than 0.02 s. Therefore, the estimation errors satisfy the demand of the range migration error.

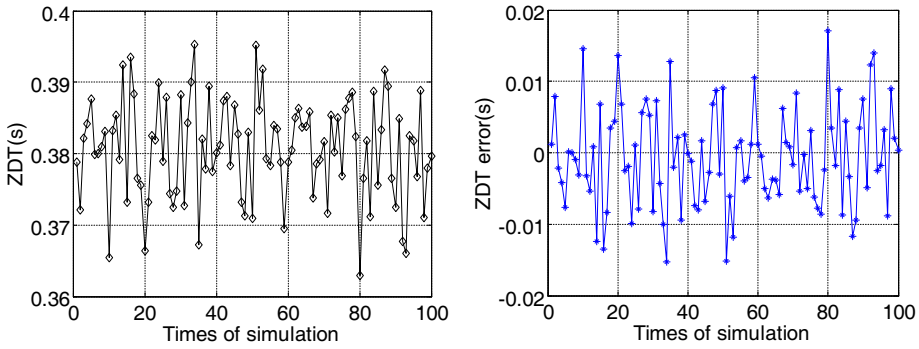

Figure 7. ZDT estimate result. (a) Estimated ZDT. (b) Estimate error of ZDT.

The direct-path signal is used as the reference signal in the range matched filtering. Then, by using the scheme of the proposed imaging algorithm, the bistatic SAR raw data are processed, and the image is shown below. The estimation error of the ZDT is about 0.011 s.

Figure 8 shows the images of the simulated point targets. As can be seen from Figure 8, all the point targets are well focused, which validates the efficiency of the imaging algorithm. Meanwhile, due to the estimation error of the ZDT, there is a shift (About 85 m) in the azimuth direction, which coincides with the value computed by $\Delta x' = k_1 v_T / k_a$.

Meanwhile, the image performances of three represent point targets (A, B, C) are listed in Table 2.

Table 2. Image performances.

	δ_R	PSLR_R	δ_A	PSLR_A
Ideal	5.25 m	−13.26 dB	1.96 m	−13.26 dB
A	5.86 m	−13.05 dB	1.97 m	−13.12 dB
B	5.27 m	−13.17 dB	2.07 m	−13.14 dB
C	5.73 m	−12.74 dB	2.12 m	−13.05 dB

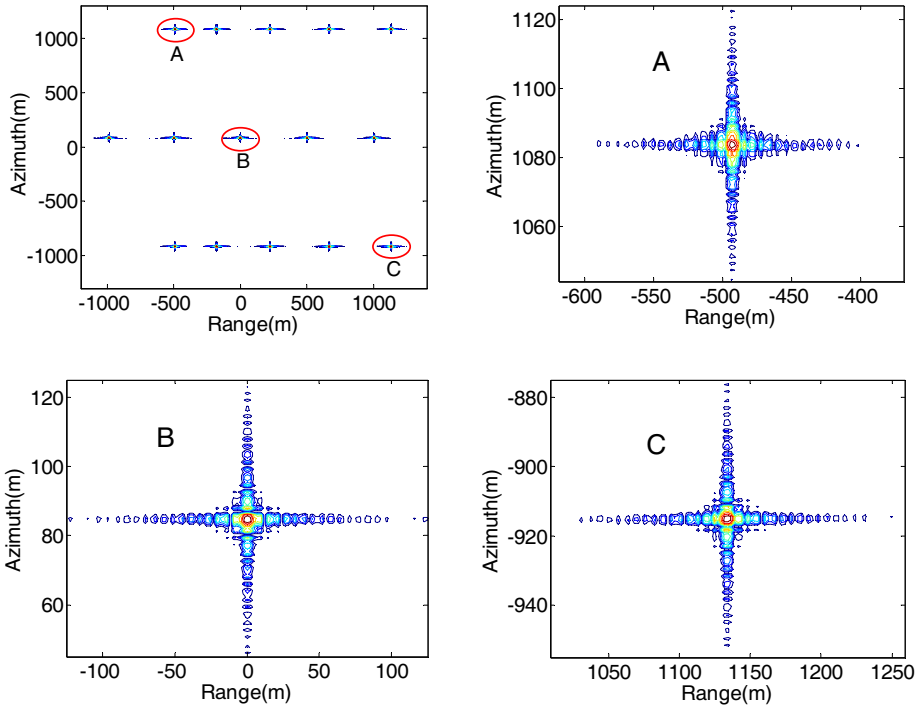

Figure 8. Images of point targets.

From Table 2, it can be seen that the range and azimuth resolutions (δ_R and δ_A) of the three represent point targets approach the ideal values quite well.

3.2. Experiment Results

In 2009, a series of bistatic SAR experiments was performed by the the SAR research group of the center for sensor systems (ZESS) [1, 2]. The DLR's TerraSAR-X/TanDEM-X satellite was used as illuminating transmitter in 300 MHz high-resolution sliding spotlight mode, and the high resolution SAR data was acquired by a stationary receiver. The radar data has been provided by ZESS, HITCHHIKER project in ⟨2015⟩ (http://hitchhiker.zess.uni-siegen.de/). The scene extension was about 3 km × 8 km. The parameters of the experiment are shown in Table 1.

The acquired data is processed along the scheme of the proposed method in Figure 6. Figure 9(a) shows the image generated by the back projection algorithm. The bistatic image is shown in Figure 9(b). Details of the focusing image are shown in Figure 10.

From Figure 9 and Figure 10, it can be seen that the proposed imaging algorithm has almost the same focusing performance as the time-domain algorithm. The advantage is that the proposed imaging algorithm is more computationally efficient than the time-domain method in a personal computer.

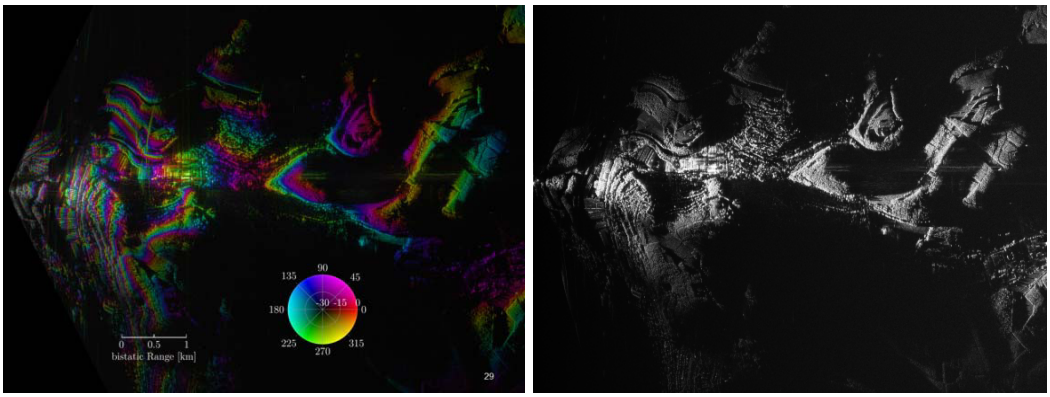

(a) (b)

Figure 9. Images of the measured data. (a) Back project image (Combined image of the interferometric phase and radar intensity). (b) Image of the proposed method.

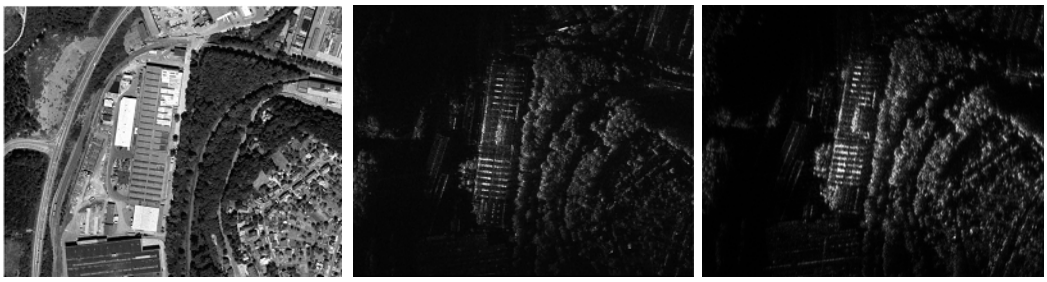

(a) (b) (c)

Figure 10. Details of the image. (a) Orthophoto. (b) Back project image. (c) Image of the proposed method.

4. CONCLUSIONS

In this paper, an efficient imaging algorithm for sliding spotlight bistatic SAR with fixed-receiver is presented. Based on azimuth preprocessing, direct-path signal compensation and nonlinear Chirp Scaling imaging algorithm, the proposed method can realize the focusing of the scene, and the imaging efficiency is greatly improved. Simulation results of point targets prove that the proposed imaging algorithm is much more efficient than the time-domain method. Finally, the proposed method is also tested successfully with the measured bistatic data of HITCHHIKER system, which further verifies the superior performance of the proposal.

ACKNOWLEDGMENT

The authors would like to thank the anonymous reviewers and the editors for their help in improving the manuscript and ZESS for providing the radar data used in this research. This work was funded by the National Natural Science Foundation of China (Grant No. 61501477).

REFERENCES

1. Behner, F. and S. Reuter, "HITCHHIKER-hybrid bistatic high resolution SAR experiment using a stationary receiver and TerraSAR-X transmitter," *European Conference on Synthetic Aperture Radar*, 1–4, Aachen, Germany, Jun. 2010.

2. Behner, F., S. Reuter, and H. Nies, "Synchronization and preprocessing of hybrid bistatic SAR data in the HITCHHIKER experiment," *European Conference on Synthetic Aperture Radar*, 268–271, Berlin, Germany, Jun. 2014.
3. Zhou, F., G. C, Sun, and M. D. Xin, "A full-aperture imaging algorithm for hybrid sliding spotlight bistatic SAR," *IET International Radar Conference*, 1–5, Xi'an, China, Oct. 2013.
4. Wang, R., Y. K. Deng, and O. Loffeld, "Processing the azimuth-variant bistatic SAR data by using monostatic imaging algorithms based on two-dimensional principle of stationary phase," *IEEE Trans. Geosci. Remote Sens.*, Vol. 49, No. 4, 3504–3520, 2011.
5. Zhou, P., Y. M. Chen, W. F. Sun, and Y. Wan, "Efficient imaging approach for spaceborne sliding spotlight synthetic aperture radar with a small squint angle," *Journal of Applied Remote Sensing*, Vol. 9, No. 3, 1–13, 2015.
6. Yan, F. F., W. G. Chang, and X. Y. Li, "Efficient simulation for fixed-receiver bistatic SAR with time and frequency synchronization errors," *Radio Engineering*, Vol. 24, No. 4, 917–926, 2015.
7. Neo, Y. L., F. G. Wong, and I. G. Cumming, "Processing of azimuth-invariant bistatic SAR data using the range Doppler algorithm," *IEEE Trans. Geosci. Remote Sens.*, Vol. 46, No. 1, 14–21, 2008.
8. Dekker, P. L., J. J. Mallorqui, P. S. Morales, and J. S. Marcos, "Phase synchronization and Doppler centroid estimation in fixed receiver bistatic SAR systems," *IEEE Trans. Geosci. Remote Sens.*, Vol. 46, No. 11, 3459–3471, 2008.
9. Krieger, G. and M. Younis, "Impact of oscillator noise in bistatic and multistatic SAR," *IEEE Geosci. Remote Sens. Lett.*, Vol. 3, No. 3. 424–428, 2006.
10. Sun, G. C., M. D. Xing, Y. Wang, and Y. F. Wu, "Sliding spotlight and TOPS SAR data processing without subaperture," *IEEE Geosci. Remote Sens. Lett.*, Vol. 8, No. 6, 1036–1040, 2006.
11. Zhang, Q. L., W. G. Chang, and X. Y. Li, "An extended NLCS algorithm for bistatic fixed-receiver SAR imaging," *European Radar Conference*, 1–5, Paris, France, Oct. 2013.
12. Wong, F. H. and T. S. Yeo, "New applications of nonlinear chirp scaling in SAR data processing," *IEEE Trans. Geosci. Remote Sens.*, Vol. 39, No. 5, 946–953, 2001.
13. Tian, W. M., T. Long, J. Yang, and X. P. Yang, "Combined analysis of time and frequency synchronization errors for BiSAR," *CIE International Conference on Radar*, 388–392, Chengdu, China, Nov. 2011.